Check for updates

Predicted superconductivity in one-dimensional A₃Hf₂B₃-type electrides†

Yulong Chen, Teng Xie, Ziqiang Chen, Zhou Cui, Cuilian Wen ID * and Baisheng Sa ID *

Inorganic electrides are considered potential superconductors due to the unique properties of their anionic electrons. However, most electrides require external high-pressure conditions to exhibit considerable superconducting transition temperatures (T_c). Therefore, searching for superconducting electrides under low or moderate external pressures is of significant research interest and importance. In this work, a series of $A_3Hf_2B_3$-type compounds (A = Mg, Ca, Sr, Ba; B = Si, Ge, Sn, Pb) were constructed and systematically studied based on density functional theory calculations. According to the analysis of the electronic structures and phonon dispersion spectrums, stable one-dimensional electrides $Ca_3Hf_2Ge_3$, $Ca_3Hf_2Sn_3$, and $Sr_3Hf_2Pb_3$, were screened out. Interestingly, the superconductivity of these electrides were predicted from electron phonon coupling calculations. It is highlighted that $Sr_3Hf_2Pb_3$ showed the highest T_c, reaching 4.02 K, while the T_c values of $Ca_3Hf_2Ge_3$ and $Ca_3Hf_2Sn_3$ were 1.16 K and 1.04 K, respectively. Moreover, the T_c value of $Ca_3Hf_2Ge_3$ can be increased to 1.96 K under 20 GPa due to the effect of phonon softening. This work enriches the types of superconducting electrides and has important guiding significance for the research on constructing electrides and related superconducting materials.

1. Introduction

The pursuit of high-temperature superconductivity is a pressing research topic. Unfortunately, most of the superconductors discovered through experiments and theory require either excessively high pressures or extremely low temperatures.[1–5] To overcome these limitations, a new class of ionic compounds, named electrides, has attracted growing attention and wide interest as novel candidates for superconductors.[6–8] Electrides are unique compounds with interstitial anionic electrons that are relatively free in the interstitial region and do not attach to the nucleus.[9] This distinctive structure confers upon electrides exceptional electron mobility, low work function, and robust electron-donating capacity, rendering them highly attractive for deployment in various areas, such as superconductivity,[10–12] as well as ferromagnetism,[13–15] catalysis,[16–18] and battery electrodes.[19–21] The exploration and development of novel electrides are still ongoing and of great interest.[22–25]

Based on the distribution of anionic electrons, electrides can be categorized into zero-dimensional (0D), one-dimensional (1D), and two-dimensional (2D).[26] For 0D electrides, the electrons are localized at specific positions, forming electron anion pairs or isolated electron anions. For 1D electrides, the electron anions can diffuse along one direction in the crystal, forming 1D electron anion chains. For 2D electride, the electron anions can diffuse along two directions, forming planar structures. C12A7:e⁻ is an example of a zero-dimensional (0D) inorganic electride and is the first stable electride at room temperature.[27,28] Ca_2N was subsequently discovered as the first two-dimensional (2D) inorganic electride, where the anionic electrons are loosely confined in the interlayer space, making Ca_2N a highly active catalyst.[29,30] Nevertheless, the synthesis of electrides has been a challenging endeavor, as only a handful of them, such as Ca_2N[19] and Y_2C,[31] have been successfully prepared owing to their inherent high reactivity, which often translates into lower stability. Among various types of electrides, 1D electrides, which exhibit electron confinement in one dimension, can enhance the thermal stability of the electride.[32] Therefore, extending the superconducting electrides to 1D may enable achieving higher superconducting transition temperatures (T_c) at lower external pressures. For example, the 1D electride Nb_5Ir_3 has been reported to exhibit a T_c of 9.4 K at ambient pressure,[33] while Y_3Si has been reported to have a T_c of 14.49 K at 50 GPa.[34] It is noteworthy that Ca_3Si has been found to have the highest T_c among 1D electrides discovered to date, with a value of 17.6 K at 100 GPa. The superconducting properties of Ca_3Si are mainly attributed to the electron–phonon coupling between the interstitial electrons and Ca atoms.[35]

In addition, the application of external pressure to materials has been theoretically and experimentally demonstrated as an effective approach to induce superconductivity or enhance the superconducting transition temperature of materials.[36–38] In the case of electrides, external pressure leads to a reduction of the

Multiscale Computational Materials Facility & Materials Genome Institute, School of Materials Science and Engineering, Fuzhou University, Fuzhou 350108, P. R. China. E-mail: clwen@fzu.edu.cn; bssa@fzu.edu.cn

† Electronic supplementary information (ESI) available. See DOI: https://doi.org/10.1039/d3ra07383a

lattice constant and distance between atoms in the crystal. This results in a change in the electron arrangement, thereby influencing the electronic structure and properties of the compound. Pressure can either bring free electrons closer or modify the interactions between electron pairs, affecting their superconducting behavior.[39] Recently, the electride Li_8Au has been predicted to possess the highest T_c among known electrides, with a value of 73.1 K at a pressure of 250 GPa.[11] Despite the fact that many electrides have demonstrated superconducting properties, the majority of them still require high pressure conditions to exhibit high T_c. Therefore, considering the excellent superconducting properties of 1D electrides under low or moderate pressure conditions, it is highly valuable to search for superconductors among 1D electrides.

In this work, by screening $A_3Hf_2B_3$-type compounds (A = Mg, Ca, Sr, Ba; B = Si, Ge, Sn, Pb) inspired by the realization of novel stable 1D electride $Ca_3Hf_2Pb_3$,[40] we predicted three additional stable one-dimensional electrides ($Ca_3Hf_2Ge_3$, $Ca_3Hf_2Sn_3$, and $Sr_3Hf_2Pb_3$) based on the results of the electron localization function (ELF), electrostatic difference potential (ESDP), band structure, partial charge density around the Fermi level, and phonon dispersions. Furthermore, the superconducting properties of three electrides at ambient pressure were analyzed. Finally, external pressure was applied to attempt to increase the superconducting transition temperature of the electrides while maintaining lattice dynamic stability.

2. Computational details

Herein, structural optimizations and ELF calculations were carried out within the density-functional theory (DFT)[41] as implemented in the Vienna *ab initio* Simulation Package (VASP)[42] and employed in conjunction with the ALKEMIE platform.[43] Considering both accuracy and computational efficiency, the Perdew–Burke–Ernzerhof generalized gradient approximation (GGA) exchange and correlation functional was used.[44] During the structural relaxations, the energy difference between sequential steps were taken to be 10^{-5} eV to ensure that the calculations were well converged. Crystal structures and isosurfaces were plotted using VESTA software.[45] For the constructed electrides, the enthalpy of formation was calculated using the following formula:

$$\Delta H_f = \frac{H(A_xHf_yB_z) - (xH(A) + yH(Hf) + zH(B))}{x + y + z} \quad (1)$$

where $H(A_xHf_yB_z)$ is the calculated enthalpy of a $A_3Hf_2B_3$-type compounds; $H(A)$, $H(Hf)$, and $H(B)$ are the enthalpies of the A, Hf, and B atoms in the most stable simple substances, respectively; x, y, and z represent the stoichiometric proportions of A, Hf, and B in a $A_3Hf_2B_3$-type compounds, respectively.

The QuantumWise Atomistix ToolKit (QuantumATK) package[46] was used to calculate the ESDP. The PBE-GGA functional was adopted to describe the exchange and correctional interactions of electrons with a linear combination of atomic

orbitals (LCAO) norm-conserving PseudoDojo pseudopotential,[47] which contains scalar relativistic and fully relativistic pseudopotentials for each element and it is shipped with multiple projectors for each angular channel to ensure high accuracy.[48] The density mesh cutoff was set to 85 Hartree, and a 7 × 7 × 7 k-point mesh was generated by the Monkhorst–Pack method with Γ symmetry. Structural optimization was executed until the maximum forces converged to 0.001 eV Å^{-1}.

We used VASP for the study of electronic structures and Quantum ESPRESSO (QE) for the superconducting calculations,[49] because this code has all the tools needed to study phonons and electron–phonon coupling (EPC) effects in the context of superconductivity. To investigate the phonon spectra and electron–phonon coupling, the density functional perturbation theory (DFPT)[50] calculations were performed with the QE package. The kinetic energy cutoffs of 70 and 700 Ry were chosen for the wavefunctions and the charge densities, respectively. The Fermi surface was also broadened by the Gaussian smearing method with a width of 0.02 eV (0.00147 Ry). Self-consistent electron density and EPC were evaluated by employing a 16 × 16 × 16 k mesh and centered 2 × 2 × 2 q mesh. The superconducting transition temperature T_c was calculated with the McMillan–Allen–Dynes formula:[51]

$$T_c = \frac{\omega_{log}}{1.2} \exp\left[-\frac{1.04(1+\lambda)}{\lambda - \mu^*(1+0.62\lambda)}\right] \quad (2)$$

where μ^* is the effective screened Coulomb repulsion constant which was set to an empirical value of 0.1.[52,53] The total EPC constant λ can be obtained either by summing the EPC constant λ_{qv} for all phonon modes in the whole BZ or by integrating the Eliashberg spectral function $\alpha^2F(\omega)$ as follows:[54]

$$\lambda = \sum_{qv} \lambda_{qv} = 2 \int \frac{\alpha^2F(\omega)}{\omega} d_\omega \quad (3)$$

$$\alpha^2F(\omega) = \frac{1}{2\pi N(\varepsilon_F)} \sum_{qv} \delta(\omega - \omega_{qv}) \frac{\gamma_{qv}}{\hbar\omega_{qv}} \quad (4)$$

where $N(\varepsilon_F)$ is the density of states at the Fermi level, ω_{qv} is the frequency of the v-th phonon mode at the wave vector q, and γ_{qv} is the phonon linewidth,

$$\gamma_{qv} = 2\pi\omega_{qv} \sum_{knn'} \left|g^{qv}_{k+qn',kn}\right|^2 \delta(\varepsilon_{kn} - \varepsilon_F)\delta(\varepsilon_{k+qn'} - \varepsilon_F) \quad (5)$$

in which $g^{qv}_{k+qn',kn}$ is an EPC matrix element, which was straightforwardly calculated from the response of the self-consistent potential to lattice distortion as:

$$g^{qv}_{k+qn',kn} = \left(\frac{\hbar}{2M\omega_{qv}}\right)^{1/2} \left\langle \psi_{k+qn'}, \left|\frac{dV_{SCF}}{du_{qv}} \cdot \varepsilon_{qv}\right| \psi_{kn} \right\rangle \quad (6)$$

The logarithmic average frequency ω_{log} is defined as:

$$\omega_{log} = \exp\left[\frac{2}{\lambda} \int \frac{d\omega}{\omega} \alpha^2F(\omega)\ln(\omega)\right] \quad (7)$$

3. Results and discussions

3.1 Crystal structure and screening process

The existence of a sufficiently large void in the crystal structure to accommodate anionic electrons is an important prerequisite for the formation of electrides.[26] As shown in Fig. 1, a void surrounded by A site atoms appears along the c-axis direction of the crystal, which is beneficial for accommodating interstitial electrons and forming electrides.[40] The design principle of our electride screening is stated as following: considering the good electron donor ability of alkaline earth metals, alkaline earth metals were chosen to replace the A site elements to act as electron donors,[35] facilitating the formation of electrides, such as Ca_2N[55] and Ca_3Si.[35] On the other hand, to reduce the attraction of anionic atoms to electrons, the electronegativity of element B should not be too strong.[35] Group IVA elements, including Si, Ge, Sn, and Pb, have moderate electronegativity (Pauling scale) ranging from 1.87 to 2.01, which is lower than that of group VA elements (the electronegativity of N and P is 3.04 and 2.19, respectively).[56] Therefore, group IVA elements were chosen to replace the B site elements.

Fig. 2 illustrates our research flow for achieve $A_3Hf_2B_3$-type electrides and superconductors. Firstly, 15 compounds were constructed by replacing A and B with alkaline earth metal elements and group IVA elements. To identify the characteristics of electrides, ELF was calculated to observe the localization of gap electrons. Herein, ELF is a suitable method for distinguishing localized electrons and electron gas, which has been used as a powerful tool for identifying electrides.[57,58] By judging the electron localization phenomenon of the compounds with ELF > 0.75, 8 compounds with obvious
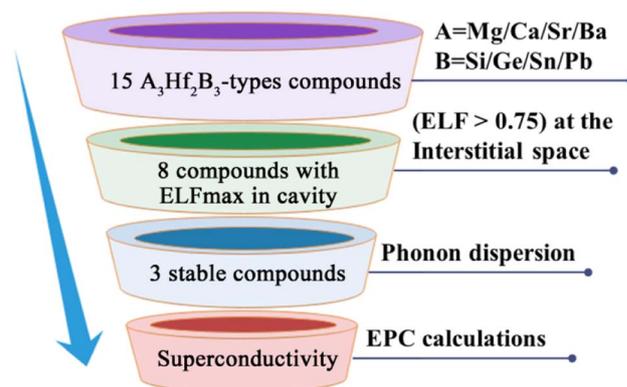

Fig. 2 The schematic illustration for the discovery of possible $A_3Hf_2B_3$-type superconducting electrides.

electron localization were initially screened, and their stability was analyzed by further phonon dispersion calculations. Through this screening process, three new stable electrides of $Ca_3Hf_2Ge_3$, $Ca_3Hf_2Sn_3$, $Sr_3Hf_2Pb_3$ were finally screened out, and their superconducting properties were further analyzed by the electron–phonon coupling calculations.

3.2 Electronic structure and stability at ambient pressure

Fig. 3 displays the preliminary screening results of the ELF with localized electronic features. The results indicate that eight compounds ($Ca_3Hf_2Si_3$, $Ca_3Hf_2Ge_3$, $Ca_3Hf_2Sn_3$, $Ba_3Hf_2Pb_3$, $Sr_3Hf_2Si_3$, $Sr_3Hf_2Ge_3$, $Sr_3Hf_2Sn_3$, and $Sr_3Hf_2Pb_3$) exhibit distinctive electron localization phenomena at the interstitial sites along the c-axis direction, indicating the potential to be 1D electrides. These eight compounds show clear 1D channels and
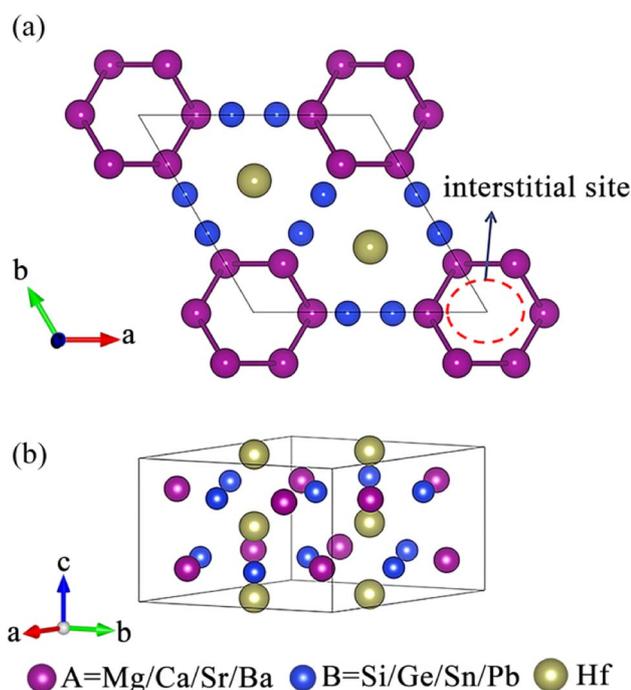

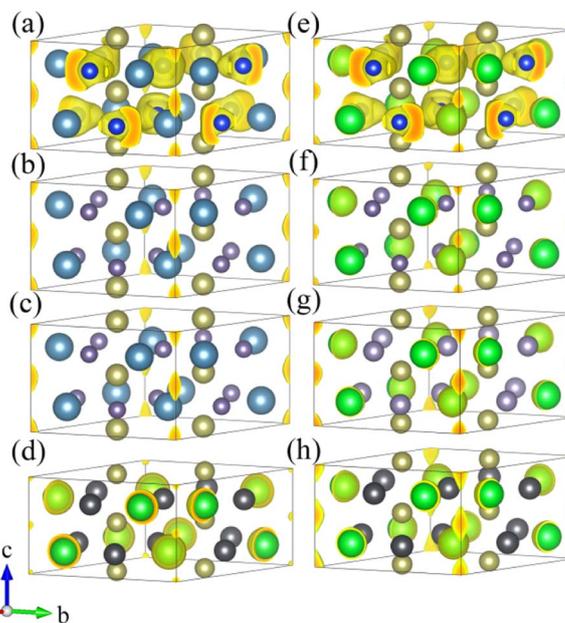Fig. 1 (a) Top and (b) side views of the crystal structure of $A_3Hf_2B_3$-type compounds.

Fig. 3 The ELF 3D plots with isosurface value of 0.75 for (a) $Ca_3Hf_2Si_3$, (b) $Ca_3Hf_2Ge_3$, (c) $Ca_3Hf_2Sn_3$, (d) $Ba_3Hf_2Pb_3$, (e) $Sr_3Hf_2Si_3$, (f) $Sr_3Hf_2Ge_3$, (g) $Sr_3Hf_2Sn_3$, and (h) $Sr_3Hf_2Pb_3$.

characteristic features of 1D electrides at ELF = 0.75. Conversely, Fig. S1† shows that the remaining seven compounds ($Ba_3Hf_2Ge_3$, $Ba_3Hf_2Si_3$, $Ba_3Hf_2Sn_3$, $Mg_3Hf_2Ge_3$, $Mg_3Hf_2Pb_3$, $Mg_3Hf_2Si_3$, and $Mg_3Hf_2Sn_3$) did not exhibit clear electron localization phenomena, implying that they lack the characteristics of electrides. Hence, our later discussion will focus on the eight compounds exhibiting localized features.

To investigate the lattice dynamic stability of the eight compounds that were preliminarily screened for localized electron phenomena, we calculated the phonon dispersion curves at 0 GPa. Fig. S2† displays the phonon dispersion results. Among the eight compounds, $Ca_3Hf_2Ge_3$, $Ca_3Hf_2Sn_3$, and $Sr_3Hf_2Pb_3$ exhibit no imaginary frequencies throughout the Brillouin zone, indicating dynamic stability at ambient pressure in Fig. S2(b), (c) and (h).† In contrast, the remaining compounds show imaginary frequencies in their phonon dispersion curves, implying instability at 0 GPa. Therefore, we conclude that

$Ca_3Hf_2Ge_3$, $Ca_3Hf_2Sn_3$, and $Sr_3Hf_2Pb_3$ have the potential to be stable electrides at 0 GPa.

To further demonstrate the electride nature of $Ca_3Hf_2Ge_3$, $Ca_3Hf_2Sn_3$, and $Sr_3Hf_2Pb_3$, we calculated the electrostatic difference potential (ESDP) to investigate the spatial charge distribution during electronic transitions that lead to electrical conductivity in real space.[59] In typical compounds, electrons are tightly bounded to atoms or molecules, making their locations challenging to figure out. However, in electrides, the electrons are dispersed and located in cavities or channels within the crystal structure, which makes it relatively easier to identify their positions.[35] Anions, which typically carry negative charges, generate a particular charge distribution in the cavities or channels, leading to a potential difference. The expression for ESDP is given by:
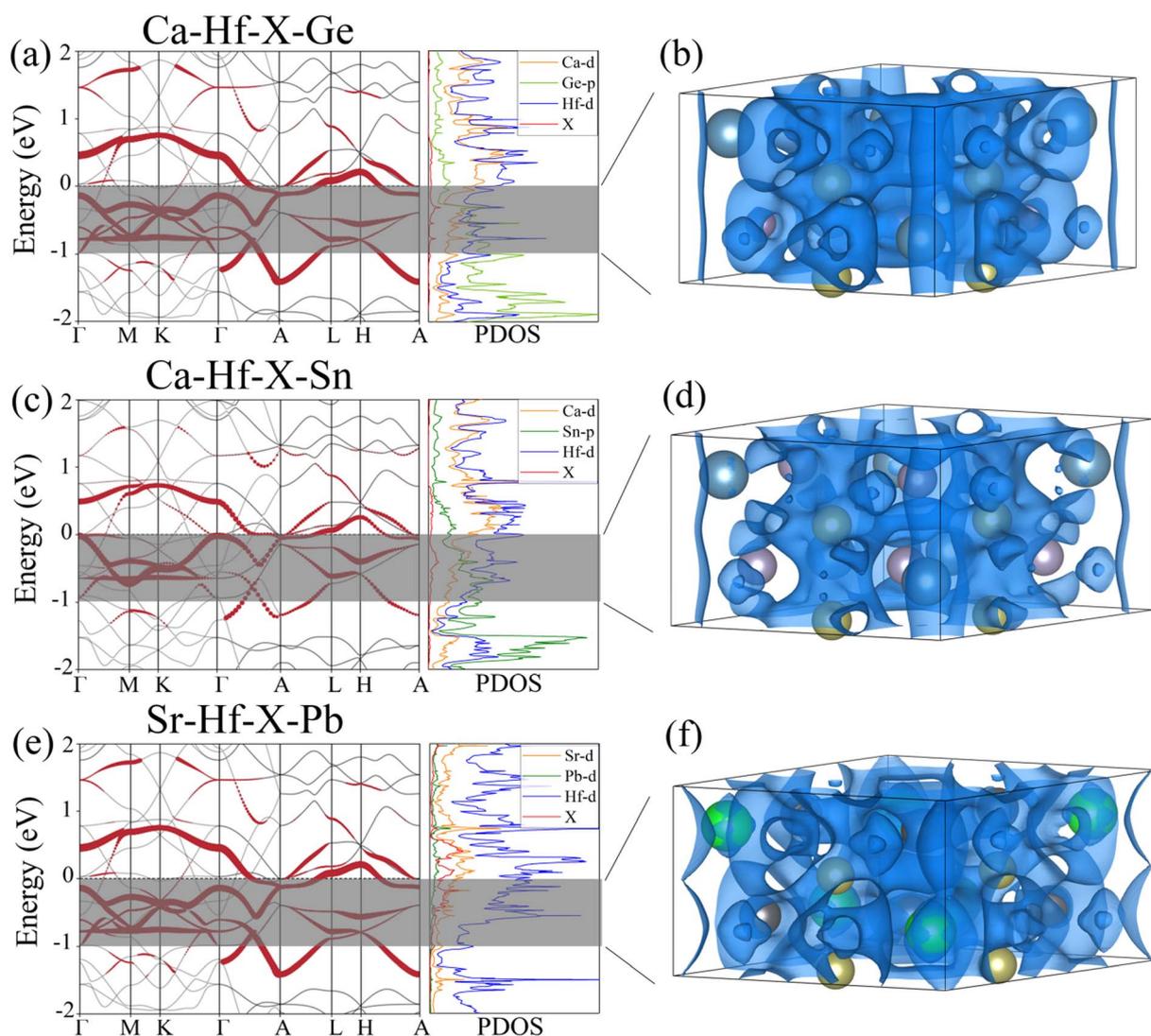
$$\Delta VE(r) = -\frac{\Delta VH(r)}{e} \tag{8}$$

Fig. 4 The projected band structures and density of states for (a) $Ca_3Hf_2Ge_3$, (c) $Ca_3Hf_2Sn_3$ and (e) $Sr_3Hf_2Pb_3$. The partial charge densities at the energy range of −1 eV to 0 eV for (b) $Ca_3Hf_2Ge_3$, (d) $Ca_3Hf_2Sn_3$ and (f) $Sr_3Hf_2Pb_3$. The isosurfaces of partial charge densities in (b), (d) and (f) are plotted at values of 0.005, 0.025, and 0.002 e Å^{-3}, respectively. The Fermi energy is set to 0 eV.

where e is the unit charge, and $\Delta VH(r)$ is the Hartree difference potential, which is the solution to the Poisson equation for the difference in electron density as:

$$\nabla^2 VH[n](r) = -\frac{e^2}{4\pi\varepsilon_0} n(r) \qquad (9)$$

where $n(r)$ is the valence electron density and ε_0 is the vacuum permittivity. Fig. S3† displays the 3D density map plot of the ESDP of the three compounds. It shows a one-dimensional electrostatic potential and electron transport channel along the edge of the unit cell, parallel to the c-axis, which shows obvious 1D characteristics. Thus, excess electrons can move easily along this one-dimensional electrostatic potential. In contrast, a significant external potential is necessary to remove electrons from the electrostatic potential perpendicular to the [001] direction. This observation further confirms that Ca_3Hf_2-Ge_3, $Ca_3Hf_2Sn_3$, and $Sr_3Hf_2Pb_3$ have the potential to be 1D electrides.

To further understand the electronic structures of three stable potential electrides, we added pseudo atoms (marked as X) to simulate the contribution of anionic electrons at the interstitial positions of $(0, 0, 0)$ and $(0, 0, 0.5)$. Then, we

calculated the corresponding projected band structures and partial density of states (PDOS). Fig. 4(a), (c) and (e) show the contribution of interstitial electrons to the band structure marked in red. The energy bands contributed by the interstitial electrons are primarily located near and cross the Fermi level, exhibiting metallic features. Combined with PDOS of the three compounds, we can see that the PDOS contributed by the interstitial electrons are mainly concentrated around the Fermi level, and the PDOS at the Fermi surface is mainly contributed by the Hf d orbitals. To visualize the contribution of interstitial electrons more intuitively, the partial charge densities were calculated within the range of -1 eV $< E - E_{\text{Fermi}} < 0$ eV, as shown in Fig. 4(b), (d) and (f). It can be seen that one-dimensional electron channels similar to those shown in the previous ESDP results appear at the interstitial positions, which further verifies the 1D electride characteristics of $Ca_3Hf_2Ge_3$, $Ca_3Hf_2Sn_3$, and $Sr_3Hf_2Pb_3$. Therefore, the above results show that $Ca_3Hf_2Ge_3$, $Ca_3Hf_2Sn_3$, and $Sr_3Hf_2Pb_3$ are stable 1D electride at 0 GPa. Table S1† lists the basic structural information and calculated formation energy values of $Ca_3Hf_2Ge_3$, Ca_3Hf_2-Sn_3, and $Sr_3Hf_2Pb_3$ for further references. They have the same hexagonal crystal structure as $Ca_3Hf_2Pb_3$, with a space group of
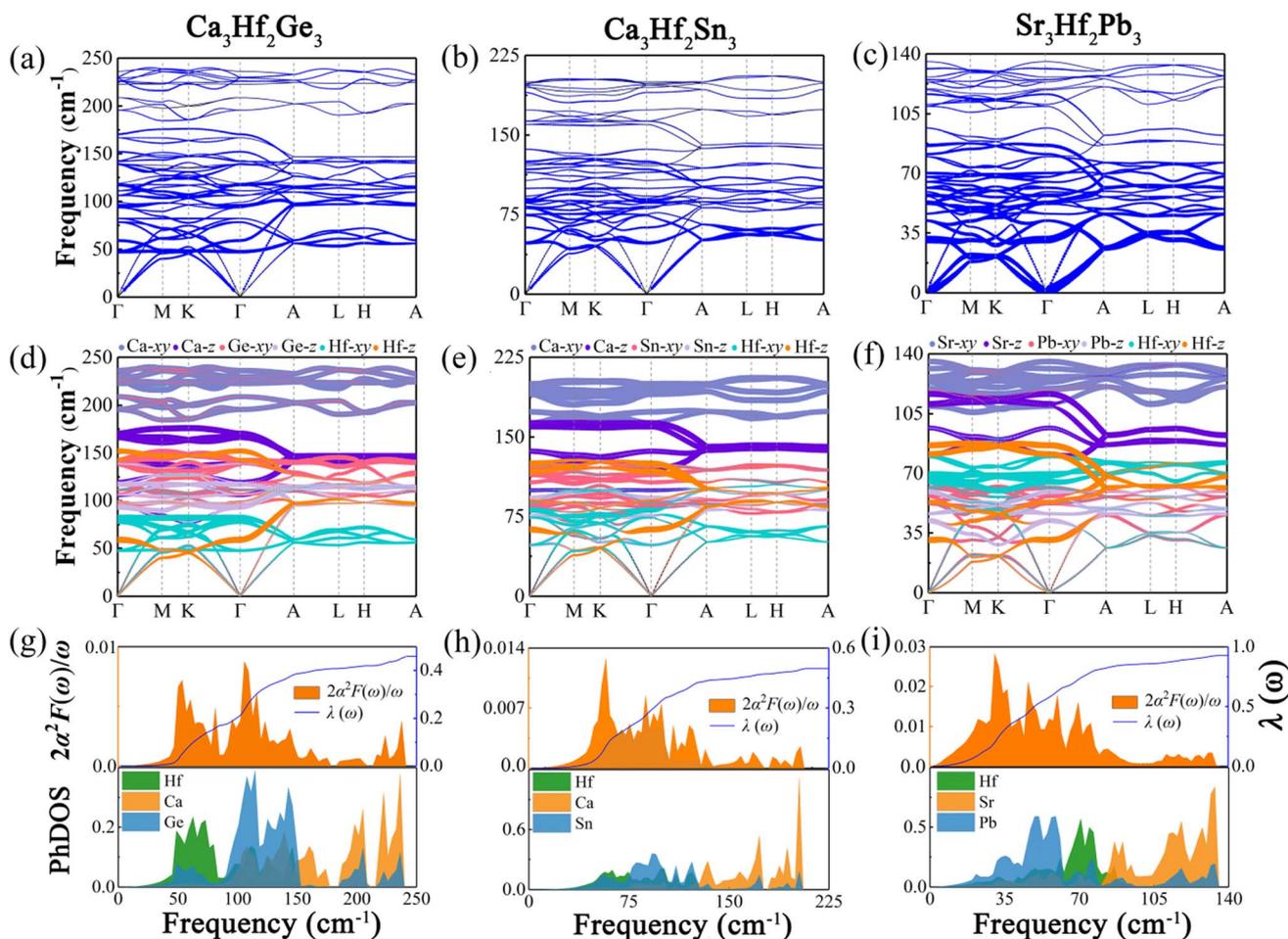

Fig. 5 The phonon dispersion curves proportional to the phonon linewidth $\gamma_{q\nu}$ for (a) $Ca_3Hf_2Ge_3$, (b) $Ca_3Hf_2Sn_3$, and (c) $Sr_3Hf_2Pb_3$. The phonon dispersion curves weighted by the vibrational modes of different atoms for (d) $Ca_3Hf_2Ge_3$, (e) $Ca_3Hf_2Sn_3$, and (f) $Sr_3Hf_2Pb_3$ at 0 GPa. The projected phonon density of states and Eliashberg spectral functions for (g) $Ca_3Hf_2Ge_3$, (h) $Ca_3Hf_2Sn_3$, and (i) $Sr_3Hf_2Pb_3$.

$P6_3/mcm$.[40] By calculating the formation energy, it is found that the formation energies of these three electrides are all negative, indicating that their formation is an exothermic process, and therefore corresponding experimental synthesis is possible.

3.3 Superconductivity at ambient pressure

To analyze the vibrational modes and calculate the superconductivity of the three novel electrides, we calculated the phonon dispersion curves weighted by the phonon linewidth γ_{qv}, along with the Eliashberg spectral function $2\alpha^2F(\omega)/\omega$ and the electron–phonon coupling coefficient $\lambda(\omega)$, as illustrated in Fig. 5. The Eliashberg spectral function is represented by the orange area, while the blue line depicts how $\lambda(\omega)$ increases by integrating the spectral function. The phonon dispersion curves weighted by the phonon linewidth γ_{qv} are presented in Fig. 5(a)–(c), where the size of the blue lines is proportional to the electron–phonon coupling contribution in that region. The observation reveals that the electron–phonon coupling of the three electrides is primarily concentrated in the middle and low-frequency modes, particularly in $Sr_3Hf_2Pb_3$. To understand the contribution of different vibrational modes to EPC, we generated the phonon dispersions distinguished by the atomic vibrational modes, as illustrated in Fig. 5(d)–(f). The investigation reveals that the high-frequency vibrational modes in the three electrides, contributed by the alkali-earth metals (Ca, Sr), are mainly associated with the in-plane vibrations (Ca-xy, Sr-xy), with the highest frequency range, while the out-of-plane vibrations (Ca-z, Sr-z) of the alkali-earth metals occupy the next highest frequency range. Vibrational modes associated with the Hf element and the IVA group elements (Ge, Sn, Pb) mainly dominate the low-to-medium frequency range. Fig. 5(g)–(i) show the Eliashberg spectral function $2\alpha^2F(\omega)/\omega$ and the phonon density of states (PhDOS) of the three electrides. By analyzing the Eliashberg spectral function, it can be observed that the entire range of the Eliashberg spectral function is similar to the phonon dispersion curve weighted by the phonon linewidth γ_{qv}. It can be roughly divided into two regions, namely, the low-to-medium frequency range and the high frequency range. For instance, in Fig. 5(i), $Sr_3Hf_2Pb_3$ exhibits distinct peaks in the low-to-medium frequency range, which diminish considerably in high frequency modes. The result of λ for $Sr_3Hf_2Pb_3$ reveals that its primary contribution (over 50%) arises from the 0 to 100 cm^{-1} in the low-to-medium frequency range, while modes in the high frequency range (above 100 cm^{-1}) contribute negligibly to the overall EPC. The final calculated λ values for $Ca_3Hf_2Ge_3$ and $Ca_3Hf_2Sn_3$ are both equal to 0.46. $Sr_3Hf_2Pb_3$ has the highest λ value, reaching 0.74. According to the McMillan–Allen–Dynes equation, the T_c values of $Ca_3Hf_2Ge_3$, $Ca_3Hf_2Sn_3$, and $Sr_3Hf_2Pb_3$ at 0 GPa are calculated to be 1.16 K, 1.04 K, and 4.02 K, respectively. Herein, $Sr_3Hf_2Pb_3$ has the highest T_c value. By analyzing the PhDOS, it can be more intuitively seen how the vibration modes of different elements contribute to the phonon dispersion. The contribution of alkali earth metals is significantly concentrated in the high frequency region, with a distinct peak in the high frequency area. On the other hand, the contributions of Hf and group IVA elements are relatively evenly distributed in the low-to-medium frequency modes. Therefore, considering the dominant position of Hf d-orbital electrons at the Fermi level, the superconductivity of the three electrides mainly comes from the electron–phonon coupling between the low-to-medium frequency modes dominated by Hf and group IVA elements vibrations and Hf d-orbital electrons.

To visualize the contribution regions of EPC, we plotted the integrated distribution within $q_z = 0$ and 0.5 planes in the first Brillouin zone (BZ), by summing up the EPC of all phonon
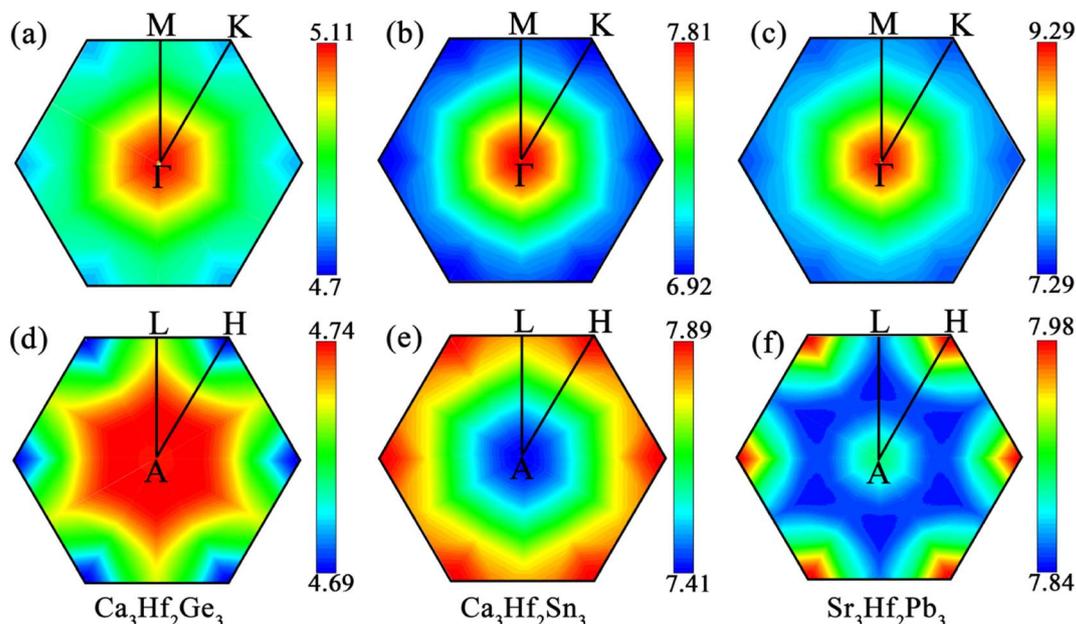

Fig. 6 The integrated EPC distributions in the plane $q_z = 0$ for (a) $Ca_3Hf_2Ge_3$, (b) $Ca_3Hf_2Sn_3$, and (c) $Sr_3Hf_2Pb_3$, and in the plane $q_z = 0.5$ for (d) $Ca_3Hf_2Ge_3$, (e) $Ca_3Hf_2Sn_3$, and (f) $Sr_3Hf_2Pb_3$, respectively.

branches on these two planes.[60,61] As shown in Fig. 6, in the $q_z = 0$ plane, the EPC integrated distribution of all three electrides is mainly concentrated near the Γ point, indicating a stronger EPC contribution near the Γ point than other positions in this plane. In the $q_z = 0.5$ plane, the EPC integrated distribution of $Ca_3Hf_2Ge_3$ is relatively concentrated around the A point, with a larger range of hotspots and a radiating shape expanding outwards. However, for $Ca_3Hf_2Sn_3$ and $Sr_3Hf_2Pb_3$, the EPC integrated distribution is mainly concentrated near the H point. Although the $q_z = 0.5$ plane exhibits different hotspot distributions, we found that the EPC integrated distribution is more evenly spread out than in the $q_z = 0$ plane, as evidenced by the numerical values on the color scale, indicating a more uniform EPC contribution in various regions on the $q_z = 0.5$ plane.

3.4 Superconductivity under external pressures

Pressure is a promising method to enhance the super-conducting transition temperature. Here, we examined the impact of pressure on the superconducting properties of three artificial electrides. Firstly, we evaluated the lattice dynamical stability of the three electrides at different pressures by computing the phonon dispersion curves, which are depicted in Fig. S4.† Specifically, Fig. S4(a), (c) and (d)† illustrate the phonon dispersion curves of $Ca_3Hf_2Ge_3$, $Ca_3Hf_2Sn_3$, and $Sr_3Hf_2Pb_3$, respectively, at pressures of 15, 12, and 9.3 GPa. Notably, no imaginary frequencies were found in the entire Brillouin zone of these electrides, suggesting their lattice dynamical stability under the corresponding pressure conditions. Nevertheless, at 20 GPa, a clear imaginary frequency appeared near the Γ point of $Ca_3Hf_2Ge_3$, indicating its instability under this pressure and rendering it unsuitable for further compression in future research.

To gain further insight into the impact of external pressure on superconductivity, we calculated the phonon dispersion weighted by the phonon linewidth $\gamma_{q\nu}$, as well as the Eliashberg spectral function $2\alpha^2F(\omega)/\omega$ and the electron–phonon coupling coefficient $\lambda(\omega)$ under selected pressures, as illustrated in Fig. 7. As shown in Fig. 7(a), under a pressure of 15 GPa, the EPC
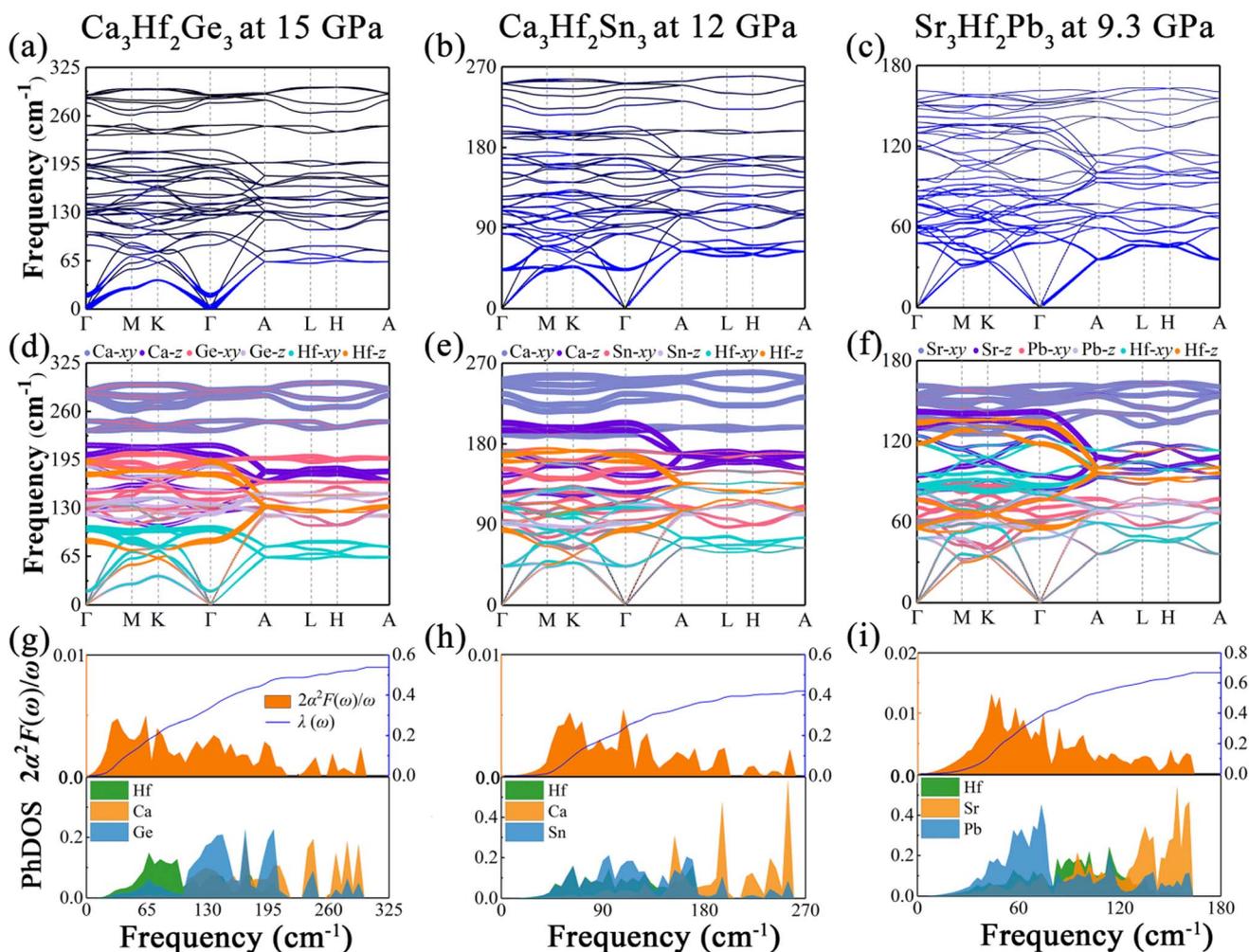

Fig. 7 The phonon dispersion curves at selective pressure proportional to the phonon linewidth $\gamma_{q\nu}$ for (a) $Ca_3Hf_2Ge_3$ at 15 GPa, (b) $Ca_3Hf_2Sn_3$ at 12 GPa, and (c) $Sr_3Hf_2Pb_3$ at 9.3 GPa. The phonon dispersion curves at selective pressure weighted by the vibrational modes of different atoms for (d) $Ca_3Hf_2Ge_3$ at 15 GPa, (b) $Ca_3Hf_2Sn_3$ at 12 GPa, and (c) $Sr_3Hf_2Pb_3$ at 9.3 GPa. The projected phonon density of states and Eliashberg spectral functions at selective pressure for (g) $Ca_3Hf_2Ge_3$ at 15 GPa, (b) $Ca_3Hf_2Sn_3$ at 12 GPa, and (c) $Sr_3Hf_2Pb_3$ at 9.3 GPa.
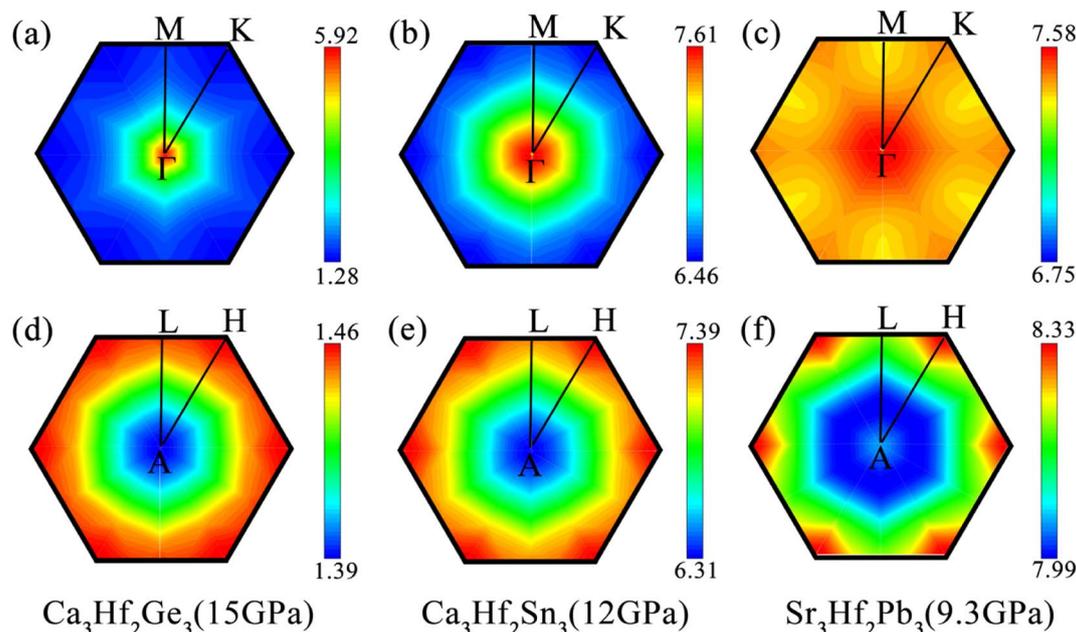
Fig. 8 The integrated EPC distributions in the plane $q_z = 0$ for (a) $Ca_3Hf_2Ge_3$ at 15 GPa, (b) $Ca_3Hf_2Sn_3$ at 12 GPa, and (c) $Sr_3Hf_2Pb_3$ at 9.3 GPa, and in the plane $q_z = 0.5$ for (d) $Ca_3Hf_2Ge_3$ at 15 GPa, (e) $Ca_3Hf_2Sn_3$ at 12 GPa, and (f) $Sr_3Hf_2Pb_3$ at 9.3 GPa, respectively.

contribution region of $Ca_3Hf_2Ge_3$ is mainly concentrated in the low frequency region, which is different from that at ambient pressure, where the EPC contribution mainly comes from the low-to-medium frequency region. In contrast, for $Ca_3Hf_2Sn_3$ and $Sr_3Hf_2Pb_3$, depicted in Fig. 7(a) and (b), the EPC contributions are still primarily located in the low-to-medium frequency modes, similar to the distribution observed at ambient pressure. Additionally, we saw a phonon softening phenomenon of $Ca_3Hf_2Ge_3$ on the Γ–M–K–Γ path ($q_z = 0$ plane), especially at the Γ point, which is not observed in the other two compounds. According to the phonon dispersion curves differentiated by vibrational modes shown in Fig. 7(d)–(f), the high-frequency modes are still dominated by the alkali metals under pressure, while the vibration modes of Hf and IVA elements stay concentrated in the low-to-medium frequency region. Based on our analysis, it appears that the softening phonon modes of $Ca_3Hf_2Ge_3$ are primarily dominated by the in-plane vibration mode of Hf (Hf-xy). Furthermore, from the Eliashberg spectral functions shown in Fig. 7(g)–(i), we observed a clear peak in the low frequency modes of $Ca_3Hf_2Ge_3$, while the peaks of $Ca_3Hf_2Sn_3$ and $Sr_3Hf_2Pb_3$ are still concentrated in the low-to-medium frequency region, and the calculated $\lambda(\omega)$ curve rapidly increases in this region. Based on the analysis of PhDOS, we found that the states in the low frequency modes of $Ca_3Hf_2Ge_3$ are mainly contributed by Hf atoms, while the results of PhDOS of the other two compounds under pressure are similar to those at 0 GPa. According to the McMillan–Allen–Dynes equation, the calculated T_c value of $Ca_3Hf_2Ge_3$ under a pressure of 15 GPa is 1.96 K, which is significantly higher than that at 0 GPa. Therefore, we conclude that the enhancement of T_c in $Ca_3Hf_2Ge_3$ under pressure mainly results from phonon softening. However, for $Ca_3Hf_2Sn_3$ and $Sr_3Hf_2Pb_3$, their T_c values

decreased to 0.71 K and 2.69 K under pressures of 12 GPa and 9.3 GPa, respectively, indicating that further increasing of the external pressure could not increase their T_c values.

To observe the distribution of EPC under external pressures, we also plotted the integrated distribution on the $q_z = 0$ and 0.5 planes in the first Brillouin zone (BZ) under different pressure, as shown in Fig. 8. It can be seen that, similar to the results at 0 GPa, the EPC integrated distributions of the three electron compounds are mainly concentrated near the Γ point on the $q_z = 0$ plane. However, on the $q_z = 0.5$ plane, the EPC integrated distributions of the three electrides are more concentrated around the H point. Except for $Ca_3Hf_2Sn_3$, the EPC integrated distributions on the $q_z = 0.5$ plane still appear more uniform compared to the $q_z = 0$ plane. For $Ca_3Hf_2Ge_3$, we can observe a significant distribution around the Γ point, which is contributed by the softening phonon mode mentioned earlier in $q_z = 0$ plane. This phenomenon further confirms that the increase in T_c value of $Ca_3Hf_2Ge_3$ under pressure is due to the contribution of phonon softening.

To gain a deeper understanding of the superconducting mechanism of $A_3Hf_2B_3$-type electrides under various pressure conditions, we investigated the superconducting transition temperature (T_c), logarithmic phonon frequency (ω_{log}), and $\lambda(\omega)$ of $Ca_3Hf_2Ge_3$, $Ca_3Hf_2Sn_3$, and $Sr_3Hf_2Pb_3$ under different pressure conditions, as shown in Fig. 9. We can see that the changes in $\lambda(\omega)$ values are consistent with those of T_c values, while ω_{log} shows an opposite trend. For the calculated compound with the highest T_c, $Sr_3Hf_2Pb_3$, also has the highest calculated $\lambda(\omega)$ value of 0.74. Conversely, for $Ca_3Hf_2Sn_3$ under 12 GPa with the smallest T_c value, its calculated $\lambda(\omega)$ is the minimum value of 0.42. To evaluate the effect of pressure on the superconducting properties of the three electrides more intuitively, Table S2†
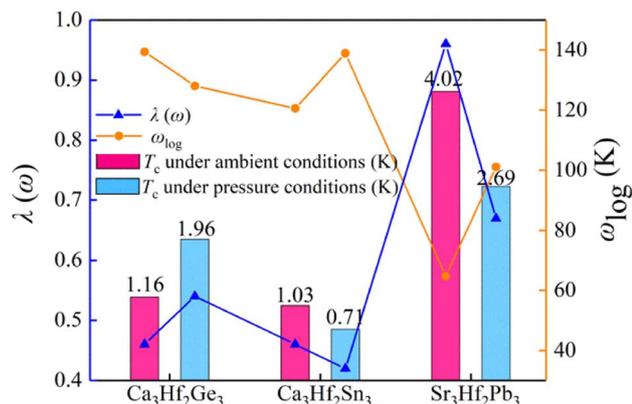
Fig. 9 The estimated superconducting transition temperature T_c, logarithmic phonon frequency $\omega_{\log}$, and $\lambda(\omega)$ for $Ca_3Hf_2Ge_3$, $Ca_3Hf_2Sn_3$, and $Sr_3Hf_2Pb_3$ under different pressure conditions.

lists the calculated λ, $\omega_{\log}$, and T_c values under selected pressures for the three electron compounds. Fig. S5† depicts the influence of various μ^* values on T_c. It is evidently that despite a significant decreasing trend in T_c values of all electrides with increasing μ^* values, the order of T_c for the selected pressures remains unchanged, irrespective of the μ^* value. It is seen that $Sr_3Hf_2Pb_3$ still exhibits the highest T_c value at 0 GPa, while $Ca_3Hf_2Sn_3$ at 12 GPa has the smallest T_c.

4. Conclusion

In summary, we have systematically investigated the electron localization function (ELF), electrostatic difference potential (ESDP), band structure, partial charge density around the Fermi level, and phonon dispersions of $A_3Hf_2B_3$-type compounds (A = Mg, Ca, Sr, Ba; B = Si, Ge, Sn, Pb) via density functional theory calculations combined with electron phonon coupling calculations. Among them, we identified three novel stable 1D electrides, $Ca_3Hf_2Ge_3$, $Ca_3Hf_2Sn_3$, and $Sr_3Hf_2Pb_3$. By calculating their electron–phonon coupling properties, the superconducting transition temperatures (T_c) of $Ca_3Hf_2Ge_3$, $Ca_3Hf_2Sn_3$, and $Sr_3Hf_2Pb_3$ were predicted to be 1.16 K, 1.04 K, and 4.02 K, respectively, and their superconducting properties were mainly derived from the electron–phonon coupling between the d-electrons of Hf and the low-to-medium frequency range vibration modes dominated by Hf and group IVA elements. Under external pressure, the T_c of $Ca_3Hf_2Ge_3$ increased to 1.96 K at 15 GPa, while the T_c of $Ca_3Hf_2Sn_3$ and $Sr_3Hf_2Pb_3$ decreased. The increase in T_c of $Ca_3Hf_2Ge_3$ was attributed to the pressure-induced phonon softening phenomenon. The analysis of the superconducting properties revealed that the trend of λ values was consistent with that of T_c, while the trend of $\omega_{\log}$ values was opposite. The value of μ^* did not affect the trend and magnitude of the changes in T_c with pressure for the three electrides.

Conflicts of interest

The authors declare no competing financial interest.

References

1 A. P. Drozdov, M. I. Eremets, I. A. Troyan, V. Ksenofontov and S. I. Shylin, *Nature*, 2015, **525**, 73–76.
2 Y. Li, J. Hao, H. Liu, Y. Li and Y. Ma, *J. Chem. Phys.*, 2014, **140**, 174712.
3 H. Liu, I. I. Naumov, R. Hoffmann, N. W. Ashcroft and R. J. Hemley, *Proc. Natl. Acad. Sci. U. S. A.*, 2017, **114**, 6990–6995.
4 J. Nagamatsu, N. Nakagawa, T. Muranaka, Y. Zenitani and J. Akimitsu, *Nature*, 2001, **410**, 63–64.
5 F. Peng, Y. Sun, C. J. Pickard, R. J. Needs, Q. Wu and Y. Ma, *Phys. Rev. Lett.*, 2017, **119**, 107001.
6 J. L. Dye, *Science*, 2003, **301**, 607–608.
7 Y. Gong, H. Li, J. Wu, X. Song, X. Yang, X. Bao, X. Han, M. Kitano, J. Wang and H. Hosono, *J. Am. Chem. Soc.*, 2022, **144**, 8683–8692.
8 X. Yang, K. Parrish, Y.-L. Li, B. Sa, H. Zhan and Q. Zhu, *Phys. Rev. B*, 2021, **103**, 125103.
9 K. Li, V. A. Blatov and J. Wang, *Adv. Funct. Mater.*, 2022, **32**, 2112198.
10 M. Miyakawa, S. W. Kim, M. Hirano, Y. Kohama, H. Kawaji, T. Atake, H. Ikegami, K. Kono and H. Hosono, *J. Am. Chem. Soc.*, 2007, **129**, 7270–7271.
11 X. Zhang, Y. Yao, S. Ding, A. Bergara, F. Li, Y. Liu, X.-F. Zhou and G. Yang, *Phys. Rev. B*, 2023, **107**, L100501.
12 X. Zhang, Y. Zhao, A. Bergara and G. Yang, *J. Chem. Phys.*, 2022, **156**, 194112.
13 L. Liu, C. Wang, S. Yi, D. K. Kim, C. H. Park and J.-H. Cho, *Phys. Rev. B*, 2019, **99**, 220401.
14 X.-L. Qiu, J.-F. Zhang, Z.-Y. Lu and K. Liu, *J. Phys. Chem. C*, 2019, **123**, 24698–24704.
15 X. Zhang, W. Meng, Y. Liu, X. Dai, G. Liu and L. Kou, *J. Am. Chem. Soc.*, 2023, **145**, 5523–5535.
16 S. H. Kang, J. Bang, K. Chung, C. N. Nandadasa, G. Han, S. Lee, K. H. Lee, K. Lee, Y. Ma and S. H. Oh, *Sci. Adv.*, 2020, **6**, 7416.
17 J. Wu, J. Li, Y. Gong, M. Kitano, T. Inoshita and H. Hosono, *Angew. Chem., Int. Ed.*, 2019, **58**, 825–829.
18 W. Li, C. Liu, C. Gu, J.-H. Choi, S. Wang and J. Jiang, *J. Am. Chem. Soc.*, 2023, **145**, 4774–4783.
19 D. L. Druffel, K. L. Kuntz, A. H. Woomer, F. M. Alcorn, J. Hu, C. L. Donley and S. C. Warren, *J. Am. Chem. Soc.*, 2016, **138**, 16089–16094.
20 S. Qi, C. Li, J. Wang, X. Song, M. Zhao and G. Chen, *J. Phys. Chem. Lett.*, 2023, **14**, 7992–7999.
21 M. Xu, C. Wang, B. J. Morgan and L. A. Burton, *J. Mater. Chem. C*, 2022, **10**, 6628–6633.

© 2023 The Author(s). Published by the Royal Society of Chemistry

22 J. Wang, K. Hanzawa, H. Hiramatsu, J. Kim, N. Umezawa, K. Iwanaka, T. Tada and H. Hosono, *J. Am. Chem. Soc.*, 2017, **139**, 15668–15680.

23 J.-Y. You, B. Gu, G. Su and Y. P. Feng, *J. Am. Chem. Soc.*, 2022, **144**, 5527–5534.

24 B. Sa, Z. Yang, Y. Zhang, Y. Si, H. Li, C. Zhu, C. Wen, B. Wu and T. Yu, *Dalton Trans.*, 2022, **51**, 16836–16844.

25 L. M. McRae, R. C. Radomsky, J. T. Pawlik, D. L. Druffel, J. D. Sundberg, M. G. Lanetti, C. L. Donley, K. L. White and S. C. Warren, *J. Am. Chem. Soc.*, 2022, **144**, 10862–10869.

26 Q. Zhu, T. Frolov and K. Choudhary, *Matter*, 2019, **1**, 1293–1303.

27 S. Matsuishi, Y. Toda, M. Miyakawa, K. Hayashi, T. Kamiya, M. Hirano, I. Tanaka and H. Hosono, *Science*, 2003, **301**, 626–629.

28 W. Meng, X. Zhang, Y. Liu, X. Dai, G. Liu, Y. Gu, E. P. Kenny and L. Kou, *Advanced Science*, 2023, **10**, 2205940.

29 K. Lee, S. W. Kim, Y. Toda, S. Matsuishi and H. Hosono, *Nature*, 2013, **494**, 336–340.

30 B. Liu, Z. Chen, R. Xiong, X. Yang, Y. Zhang, T. Xie, C. Wen and B. Sa, *Chin. Chem. Lett.*, 2023, **34**, 107643.

31 X. Zhang, Z. Xiao, H. Lei, Y. Toda, S. Matsuishi, T. Kamiya, S. Ueda and H. Hosono, *Chem. Mater.*, 2014, **26**, 6638–6643.

32 Y. Zhang, Z. Xiao, T. Kamiya and H. Hosono, *J. Phys. Chem. Lett.*, 2015, **6**, 4966–4971.

33 Y. Zhang, B. Wang, Z. Xiao, Y. Lu, T. Kamiya, Y. Uwatoko, H. Kageyama and H. Hosono, *npj Quantum Mater.*, 2017, **2**, 45.

34 J. Zhang, G. Chen and H. Liu, *J. Phys. Chem. Lett.*, 2021, **12**, 10388–10393.

35 B. Sa, R. Xiong, C. Wen, Y.-L. Li, P. Lin, Q. Lin, M. Anpo and Z. Sun, *J. Phys. Chem. C*, 2020, **124**, 7683–7690.

36 K. Yang, W. Cui, J. Hao, J. Shi and Y. Li, *Phys. Rev. B*, 2023, **107**, 024501.

37 J.-G. Si, W.-J. Lu, Y.-P. Sun, P.-F. Liu and B.-T. Wang, *Phys. Rev. B*, 2022, **105**, 024517.

38 M. Xu, Y. Li and Y. Ma, *Chem. Sci.*, 2022, **13**, 329–344.

39 Q. Wang, S. Zhang, H. Li, H. Wang, G. Liu, J. Ma, H. Xu, H. Liu and Y. Ma, *J. Mater. Chem. A*, 2023, **11**, 21345–21353.

40 K. Li, Y. Gong, J. Wang and H. Hosono, *J. Am. Chem. Soc.*, 2021, **143**, 8821–8828.

41 P. Hohenberg and W. Kohn, *Phys. Rev.*, 1964, **136**, B864–B871.

42 G. Kresse and J. Furthmüller, *Phys. Rev. B: Condens. Matter Mater. Phys.*, 1996, **54**, 11169–11186.

43 G. Wang, L. Peng, K. Li, L. Zhu, J. Zhou, N. Miao and Z. Sun, *Comput. Mater. Sci.*, 2021, **186**, 110064.

44 J. P. Perdew, K. Burke and M. Ernzerhof, *Phys. Rev. Lett.*, 1996, **77**, 3865.

45 K. Momma and F. Izumi, *J. Appl. Crystallogr.*, 2011, **44**, 1272–1276.

46 S. Smidstrup, T. Markussen, P. Vancraeyveld, J. Wellendorff, J. Schneider, T. Gunst, B. Verstichel, D. Stradi, P. A. Khomyakov and U. G. Vej-Hansen, *J. Phys.: Condens. Matter*, 2019, **32**, 015901.

47 V. Blum, R. Gehrke, F. Hanke, P. Havu, V. Havu, X. Ren, K. Reuter and M. Scheffler, *Comput. Phys. Commun.*, 2009, **180**, 2175–2196.

48 B. Sa, X. Shen, S. Cai, Z. Cui, R. Xiong, C. Xu, C. Wen and B. Wu, *Phys. Chem. Chem. Phys.*, 2022, **24**, 15376–15388.

49 P. Giannozzi, S. Baroni, N. Bonini, M. Calandra, R. Car, C. Cavazzoni, D. Ceresoli, G. L. Chiarotti, M. Cococcioni, I. Dabo, A. Dal Corso, S. de Gironcoli, S. Fabris, G. Fratesi, R. Gebauer, U. Gerstmann, C. Gougoussis, A. Kokalj, M. Lazzeri, L. Martin-Samos, N. Marzari, F. Mauri, R. Mazzarello, S. Paolini, A. Pasquarello, L. Paulatto, C. Sbraccia, S. Scandolo, G. Sclauzero, A. P. Seitsonen, A. Smogunov, P. Umari and R. M. Wentzcovitch, *J. Phys.: Condens. Matter*, 2009, **21**, 395502.

50 A. D. Becke, *J. Chem. Phys.*, 1992, **96**, 2155–2160.

51 P. B. Allen, *Phys. Rev. B: Solid State*, 1972, **6**, 2577–2579.

52 K.-H. Lee, K. J. Chang and M. L. Cohen, *Phys. Rev. B: Condens. Matter Mater. Phys.*, 1995, **52**, 1425–1428.

53 C. F. Richardson and N. W. Ashcroft, *Phys. Rev. Lett.*, 1997, **78**, 118–121.

54 G. Eliashberg, *Soviet Physics – JETP*, 1960, **11**, 696–702.

55 H. Tang, B. Wan, B. Gao, Y. Muraba, Q. Qin, B. Yan, P. Chen, Q. Hu, D. Zhang, L. Wu, M. Wang, H. Xiao, H. Gou, F. Gao, H.-k. Mao and H. Hosono, *Adv. Sci.*, 2018, **5**.

56 L. Pauling, *J. Am. Chem. Soc.*, 1932, **54**, 3570–3582.

57 Y. Ma, M. Eremets, A. R. Oganov, Y. Xie, I. Trojan, S. Medvedev, A. O. Lyakhov, M. Valle and V. J. N. Prakapenka, *Nature*, 2009, **458**, 182–185.

58 M. s. Miao and R. Hoffmann, *J. Am. Chem. Soc.*, 2015, **137**, 3631–3637.

59 A. L. Despotuli and A. V. Andreeva, *J. Electroanal. Chem.*, 2018, **829**, 1–6.

60 Y. Han, Y. Li, L. Yang, H. Liu, N. Jiao, B. Wang, H. Lu and P. Zhang, *Mater. Today Phys.*, 2023, **30**, 100954.

61 P. Liu, F. Zheng, J. Li, J. Si, L. Wei, J. Zhang and B. Wang, *Phys. Rev. B: Condens. Matter Mater. Phys.*, 2022, **105**, 245420.